D. A. Belyaev[1], A. A. Fedorova[1], A. Trokhimovskiy[1], J. Alday[2], O. I. Korablev[1], F. Montmessin[3], E. D. Starichenko[1], K. S. Olsen[4], and A. S. Patrakeev[3]

[1]Space Research Institute (IKI), Moscow, Russia.

[2]School of Physical Sciences, The Open University, UK.

[3]LATMOS/CNRS, Paris, France.

[4]Department of Physics, University of Oxford, UK.

Corresponding author: Denis Belyaev (dbelyaev@iki.rssi.ru)

Key Points:

- Seasonal variability of the Martian atmosphere' thermal structure at altitudes 20-180 km are reported from CO_2 infrared spectroscopy
- The mesopause altitude rises from 70-90 km in the high-winter latitudes to 130-150 km in the summer season for both hemispheres
- The homopause altitude varies from 80 km at aphelion to 110 km at perihelion in the Martian years 34 and 35, and it depends on dust activity.

Abstract

Temperature and density in the upper Martian atmosphere, above ~100 km, are key diagnostic parameters to study processes of the species' escape, investigate the impact of solar activity, model the atmospheric circulation, and plan spacecraft descent or aerobraking maneuvers. In this paper, we report vertical profiling of carbon dioxide (CO_2) density and temperature from the Atmospheric Chemistry Suite (ACS) solar occultations onboard the ExoMars Trace Gas Orbiter (TGO). A strong CO_2 absorption band near 2.7 μm observed by the middle infrared spectrometric channel (ACS MIR) allows the retrieval of the atmospheric thermal structure in an unprecedentedly large altitude range, from 20 to 180 km. We present the latitudinal and seasonal climatology of the thermal structure for 1.5 Martian years (MYs), from the middle of MY 34 to the end of MY 35. The results show the variability of distinct atmospheric layers, such as a mesopause (derived from 70 to 150 km) and homopause, changing from 80-90 km at aphelion to 100-110 km at perihelion. Some short-term homopause fluctuations are also observed depending on the dust activity.

Plain Language Summary

We report vertical distributions of the density and temperature in the Martian atmosphere in the altitude range from 20 to 180 km. This broad interval of heights embraces regions of the troposphere (<50 km), the mesosphere (50-100 km) and the thermosphere (>100 km). Knowledge of thermal structure in the middle and upper atmosphere (above 50 km) is unique for the Martian climate modeling, studying the atmospheric escape and the impact of solar activity, as well as planning spacecraft maneuvers. Our data are based on remote measurements of the carbon dioxide (CO_2) absorption in the atmosphere

at very high altitude detailing of one kilometer. Sensing this major component, 95% of the total density, in the infrared wavelength range allows us to derive the atmospheric temperature as well. We observe the climatology of different atmospheric layers depending on latitude and seasons for 1.5 Martian years, from May 2018 to January 2021. For example, we reveal extremely high variability of the coldest layer, mesopause, from 70 km in the southern winter to 150 km in the southern summer.

1 Introduction

The middle and upper atmosphere of Mars, occupying altitudes above ~50 km, includes the mesosphere (60-100 km) and thermosphere, extending higher than ~100 km. This altitude range hosts the temperature minimum of the mesopause at 90-120 km, and the homopause, 10-20 km higher, where the atmosphere is no longer uniformly mixed (Bougher et al., 2017a). Here, solar ultraviolet (UV) radiation effectively dissociates CO_2 molecules forcing a decrease of its mixing ratio with altitude from 95% to <30% at 170-200 km. At the same time, the mixing ratio of O atoms and CO molecules tends to rise with altitude, holding less dominant mass than the heavier CO_2. Above 200 km, the exobase is the boundary between the collisional and the collisionless atmosphere. Its altitude varies from 200 to 250 km depending on the solar UV flux and the dust loading (Montabone et al., 2015; Fu et al., 2020). In parallel, up-to-date thermospheric models are able to describe how the temperature of the upper atmosphere is affected by temporal variability (diurnal, seasonal) and by solar activity (Bougher et al., 2015a; González-Galindo et al., 2015). The energy to the thermosphere is also supplied by the global circulation and vertical atmospheric waves (González-Galindo et al., 2015; Medvedev et al., 2015). According to models, all the mentioned factors provoke a wide range of temperature variations in the upper thermosphere: from 150 to 350 K.

A number of experiments have explored the structure and dynamics of the Martian upper atmosphere for a few decades: either *in situ* or using the orbital limb sounding in emission or absorption spectrometry. Among the *in situ*, the accelerometry profiles of integrated density were measured on board entry probes, Mars-6 (Avduevskiy et al., 1975) and Viking 1&2 (Seiff and Kirk, 1977) in the 1970ies, as well as Mars Pathfinder in 1997 (Withers at el., 2003). During the Viking descents, the temperature and density of major constituents were also probed by the neutral mass-spectrometers (Nier and McElroy, 1976; 1977). At the turn of the century, aero-braking campaigns of Mars Global Surveyor (MGS), Mars Odyssey, and Mars Reconnaissance Orbiter (MRO) spacecrafts resulted in the first prolonged dataset describing the thermospheric temperature and density variations (Keating et al., 1998; Withers, 2006; Bougher et al., 2017a). The Spectroscopy for Investigation of Characteristics of the Atmosphere of Mars (SPICAM) instrument on board Mars Express sounded the mesospheric and thermospheric altitudes (30-150 km) in stellar occultations in the UV CO_2 absorption band (110-200 nm) (Quemerais et al., 2006; Forget et al., 2009). SPICAM has also revealed several cases of the CO_2 supersaturation

condition around the mesopause, observed together with detached aerosol layers interpreted as CO_2 ice clouds forming below 100 K (Montmessin et al., 2006).

A new era of thermosphere climatology has begun with the Mars Atmosphere and Volatile EvolutioN (MAVEN) orbiter, exploring the upper atmosphere since 2014. The Neutral Gas and Ion Mass Spectrometer (NGIMS) (Bougher et al., 2017b; Stone et al., 2018) and the accelerometer (ACC) (Zurek et al., 2017) measured the density in-situ down to 120 km during regular "deep dip" maneuvers (Bougher et al., 2015b). Remotely, the Imaging Ultraviolet Spectrograph (IUVS) sounded the atmospheric structure either from the limb UV dayglow (Jain et al., 2015, 2021) or nightside stellar occultations (Gröller et al., 2018). IUVS observed limb airglow of the $CO_2{}^+$ UV doublet at 290 nm and, as a result, derived mesospheric and thermospheric inter-annual variations of the temperature from January 2015 to July 2020 that covered three Martian Years (MYs), from the MY 32 perihelion ($L_S = 250°$) to the MY 35 perihelion seasons (Jain et al., 2021). Star occultations were performed with a broad spatial coverage for longitude, latitude, local time, and season, from March 2015 ($L_S = 315°$, MY 32) to April 2018 ($L_S = 165°$, MY 34), and counting >600 temperature altitude profiles in the range 20-140 km with the vertical sampling better than 6 km. Based on this dataset, Nakagawa et al., (2020a) published climatology of the vertical atmospheric wave activity. These measurements have also revealed a warm layer in the nightside low-latitude mesosphere (70-90 km) during the northern summer (Nakagawa et al., 2020b), interpreted as upward-propagating gravity waves. One more data set, from the MAVEN Extreme Ultraviolet Monitor (EUVM) solar occultations, revealed the density and temperature variations in the thermosphere (120–200 km) depending on solar EUV radiation (Thiemann et al., 2018).

The ExoMars Trace Gas Orbiter (TGO) was inserted into orbit in October 2016. The spacecraft performed an aero-braking campaign from March 2017 to February 2018 while the onboard accelerometers were measuring the density variations in the lower thermosphere (100-130 km, Jesch et al., 2019; Forbes et al., 2021; Siddle et al., 2021). The nominal TGO science mission began just after, in April 2018, with sensitive atmospheric measurements of strong CO_2 absorption bands in the solar occultation mode by high resolution infrared (IR) spectrometers (Korablev et al., 2018; Vandaelle et al., 2018).

In this paper, we report highly sensitive measurements of the temperature and density vertical distribution using the Atmospheric Chemistry Suite (ACS) on board TGO in the regime of solar occultation (Korablev et al., 2018). The middle-IR channel (ACS MIR) has been performing the experiment since April 2018 in the spectral range from 2.3 to 4.2 µm with a resolving power exceeding 25,000. The instrument senses the CO_2 absorption band around 2.7 m in an extremely wide altitude range, from 20 to 180 km, covering the troposphere, the mesosphere and the thermosphere of Mars. In this paper, we describe a scheme of the temperature and density retrievals validated with simultaneous measurements of the CO_2 band at 1.58 m by the near-IR channel (ACS NIR) below

100 km (Fedorova et al., 2020). The presented observations include more than 600 vertical profiles spreading over 1.5 Martian Years (MYs), from the middle of MY 34 to the end of MY 35. The dataset allows observing long-term and latitudinal variations of the thermal structure in the middle-upper atmosphere (above ~40 km) at the dawn and dusk terminators. The altitude resolution of the retrieved profiles, 1-3 km, reveals the vertical wave fluctuations in the atmosphere and allows the characterization of their parameters, depending on seasons (Starichenko et al., 2021).

2 ACS MIR Solar Occultation Measurements

2.1 Description of the ACS MIR spectra

ACS is a set of three IR spectrometers devoted to study chemical composition as well as aerosol and thermal structure of the Martian atmosphere on board the ExoMars TGO mission (Korablev et al., 2018). ACS MIR is a cross-dispersion echelle spectrometer dedicated to solar occultation measurements in the 2.3–4.3 m wavelength range. Each occultation session is performed at one of ten angular positions of the MIR secondary grating that disperses and spatially separates about 10-15 echelle diffraction orders. These are recorded simultaneously with an HgCdTe focal plane array (FPA) that is 640×512 pixels. The spectral range of interest, 2.66-2.7 m, lies within the diffraction orders #222 and #223 at the secondary grating position #4. One order covers a spectral interval of about 30 cm^{-1} (~25 nm); a spectrum is dispersed along 640 elements with a spectral sampling of 0.05 cm^{-1} and the resolving power / reaching ~25,000 (that is ~0.15 cm^{-1} of spectral resolution). In the occultation field-of-view (FOV), the instrumental rectangular slit cuts a part from the solar disk, so that one order occupies a stripe with about 20 FPA rows. In such a manner, the consequence of orders are located on the matrix as stripe-by-stripe, one above the other, with some dark rows between them (see in Trokhimovskiy et al. (2020), Alday et al. (2021b)). For our analysis, we selected just one row from each of two adjacent stripes correspondent to the orders #222 and #223. The considered rows relate to the highest signal-to-noise ratio (SNR) in order #223 and to minimum "doubling" effect (double Gaussian ILS) in order #222 (Alday et al., 2019; Olsen et al 2021b).

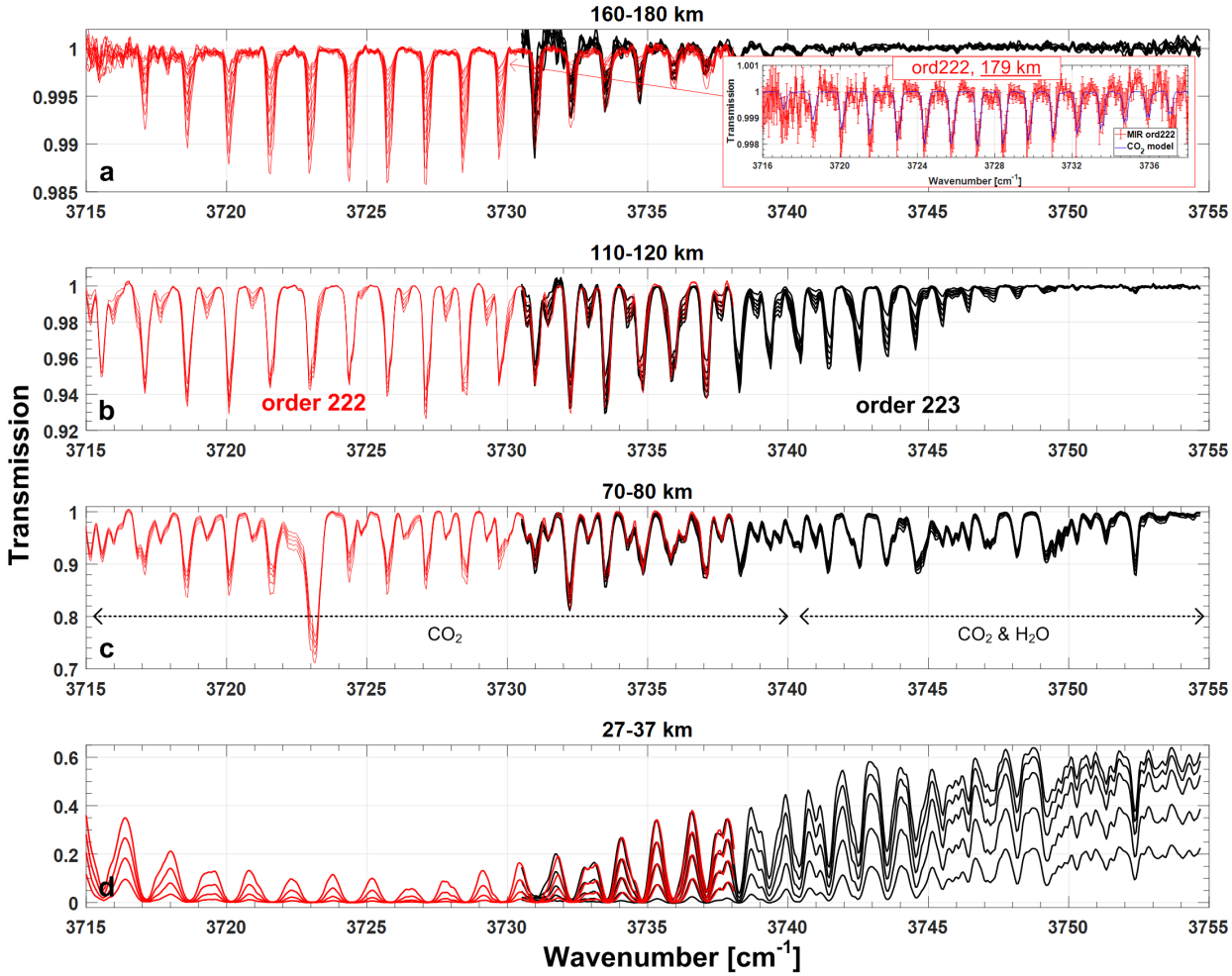

Figure 1. Set of transmission spectra measured by ACS MIR during one occultation at the orders #222 (in red) and #223 (in black) on the tangential altitude ranges 160-180 km (**a**), 110-120 km (**b**), 70-80 km (**c**), and 27-37 km (**d**). An individual spectrum with error bars in the red frame on panel **a** is one from the order #222 measured at 179 km and compared with a corresponding CO_2 model (in blue) (see section 3). The data are taken from the orbit 3820n2 (October 1 2018, MY 34, $L_S = 260.9°$, latitude -55.3°, longitude 53.9°, local lime 20.8).

The data to be analyzed is a set of transmissions spectrally registered and calibrated separately for every occultation with the corresponding ancillary geometry information for each spectrum (Fig. 1). Geometrical coordinates of the observed target (tangential) point are calculated at the closest distance from the surface to the instrument's line-of-sight (LOS). The transmission is obtained by

division of the solar spectrum passed through the atmosphere to the reference spectrum, which is measured above the tangential altitude of 200 km, where an influence of the atmospheric absorption at 2.7 m is insensitive for the instrument. Depending on the integration time (~1 s), on the occultation duration and geometry, atmospheric spectra are measured with an altitude sampling ranging from 0.5 to 2.5 km, which provides well-resolved vertical profiling for an atmosphere whose scale height is around 10 km. The ACS MIR FOV projected at the limb is estimated at around 1-3 km in terms of altitude.

Spectral calibration for measured transmissions includes a pixel-to-wavenumber alignment and a determination of the instrumental line shape (ILS). Both procedures were performed for each MIR order independently since dispersion of light onto the FPA varied from row-to-row. The details for the order #223 are presented in papers by Belyaev et al. (2021) and Alday et al. (2021a), dedicated to the retrieval of water vapour abundance. For order #222, the algorithm was analogous, using spectra above 100 km (Fig. 1a, 1b) where CO_2 absorption lines are thin (in the low-pressure atmosphere) and still deep enough for the precise calibration. In Figure 1, both calibrated ACS MIR orders are bonded in one set of spectra with an intersection between 3731 and 3738 cm^{-1}. Spectral parts towards the side of the FPA of all orders are noisy (i.e. 3715-3717 cm^{-1} for #222 and 3731-3733 cm^{-1} for #223 in Figure 1a) because the blaze function of the echelle grating gives respectively low SNR onto the edges of FPA. The central parts are clearer, and the SNR varies between 1000 and 5000, which corresponds to transmission uncertainties below 0.001 (Fig. 1a).

2.2 Data coverage

The analyzed measurements cover a period of 1.5 Martian years, the second half of MY 34 and the whole of MY 35, that correspond to ACS MIR observations from May 2018 to January 2021. The selected data set (all the secondary grating position #4 observations) comprises 308 occultation sessions in the Northern Hemisphere and 301 sessions in the Southern Hemisphere, encompassing seasonal periods from L_S = 180° to 355° in MY 34 from L_S = 2° to 356° in MY 35. Due to the solar occultation geometry the instrument's LOS tangentially crosses the planetary terminator either at sunset or at sunrise, sounding morning and evening twilight of the atmosphere (Fig. 2a). Geography of the target point varies slowly during one occultation, less than 3° of latitude or longitude. Thus, we estimate the coordinates averaging them over the tangential altitudes from 0 to 200 km. The observations are mainly concentrated at high latitudes, 40°-80°, in both hemispheres, while the longitudinal distribution of the target points is uniform over the planet (Fig. 2b). The latitudinal coverage depending on the solar longitude is presented in Figure 2c, characterizing the seasons of MY 34 and MY 35 perihelion (L_S = 240°-300°), and MY 35 aphelion (L_S = 60°-120°) with in-between Martian seasons.

The investigated seasons were accompanied by different dust events: the GDS at L_S = 190°-240° in MY 34, the C storms at L_S = 320°-330° in both MY 34 and 35, and the B storm at L_S = 240°-270° in MY 35. The regional B and C

storms covered almost the whole Southern Hemisphere and the low latitudes of the Northern one (gray frames in Figure 2c) as seen from the Mars Climate Sounder observations presented by Montabone et al. (2020) and Olsen et al. (2021). The A storm, which took place at L_S = 210-230 in MY 31 and described by Kass et al. (2016), had no noticeable magnitude in MY 35 to be considered.

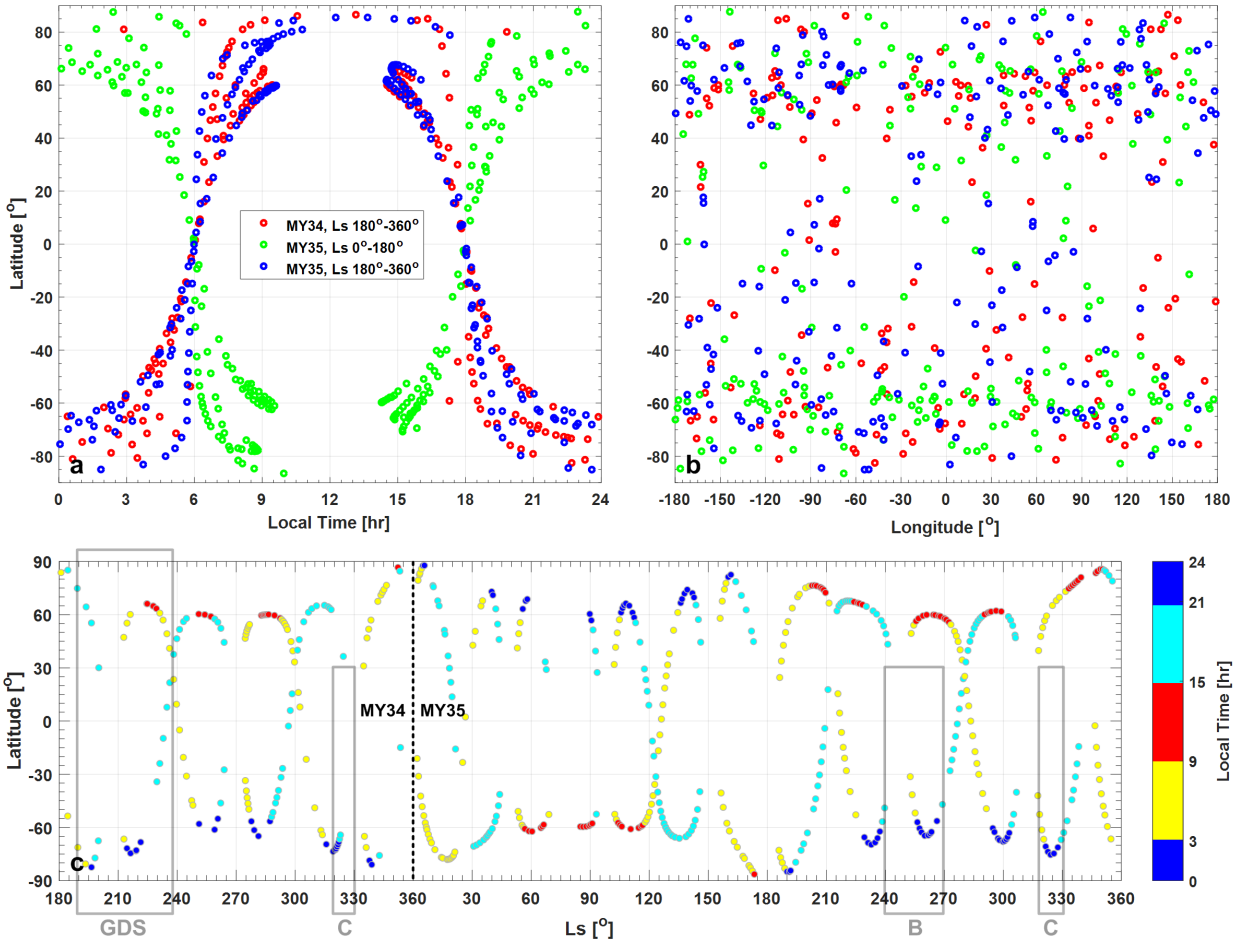

Figure 2. Geographical distributions of the target points for the ACS-MIR solar occultations at the grating position #4 with a 2.7 m band. The coordinates are latitude versus local lime (**a**), longitude (**b**), and solar longitude, L_S, (**c**). The data in panels a and b are combined in annual periods: second half of MY 34 (red), first half of MY 35 (green), second half of MY 35 (blue). The data at panel **c** are colored by intervals of local time in hours (hr): 3-9 hr (yellow), 9-15 hr (red), 15-21 hr (purple), 21-3 hr (blue). Each bubble corresponds to one occultation with related coordinates of the tangential point. Gray frames in c

outline periods of the global dust storm (GDS) and the C storm in MY 34, and the B, C storms in MY 35.

3 Retrievals of CO_2 density and temperature

3.1. CO_2 spectroscopy at 2.7 m

The selected CO_2 absorption lines, the short wavelength part of the 2.7 m band, lie in the ACS MIR echelle orders #222, with the strongest transitions at 3715-3737 cm^{-1}, and #223 at 3732-3755 cm^{-1} (Fig. 3). These lines are partially mixed with H_2O (and its isotopologues) structures considered presently as well as in the previous ACS MIR retrievals by Belyaev et al. (2021) and Alday et al. (2021a). Figure 3 shows absorption cross sections, , of CO_2 and H_2O in our spectral range of interest, including rotational lines with intensities significantly dependent on temperature. The cross sections were calculated line-by-line based on the HITRAN2016 database (Gordon et al., 2017) with self-broadening for CO_2 lines. The broadening parameters of the CO_2-rich atmosphere for the water lines were taken from Gamache et al. (2016) and Devi et al. (2017). The cross section derivatives in Figure 3b demonstrate the various temperature behaviors of the major considered lines, possessing either positive or negative signs. Thanks to that, an independent and simultaneous retrieval of temperature and molecular concentrations is possible.

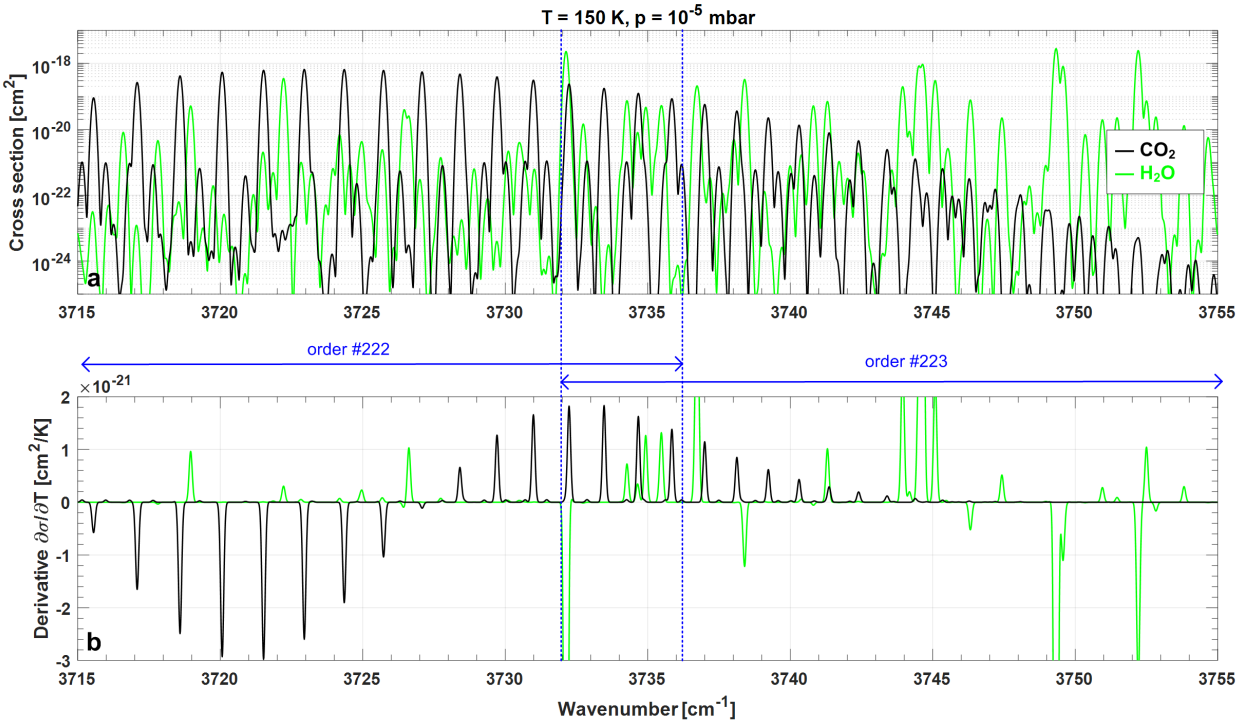

Figure 3. Absorption spectroscopy at the 2.66-2.69 m wavelength range. **a**: Cross sections, , for molecules of CO_2 (in black) and H_2O (in green) convolved by the instrumental line shape. **b**: Partial derivatives of cross section with respect to temperature ($/ T$). Cross sections were calculated for the temperature T = 150 K and pressure $p = 10^{-5}$ mbar, typical for the upper mesosphere at ~100 km.

3.2 Retrieval concept

In order to simultaneously derive density and temperature at a specified altitude, we applied a multi-iteration scheme by fitting a modeled transmission spectrum to the measured one. The details of this method are described in the Supporting Information of Belyaev et al. (2021). The transmission spectrum is calculated using well-known Beer-Lambert law, taking into account all altitude layers above the considered one. Free parameters of the fitting are temperature, mixing ratio of CO_2 and H_2O, and the aerosol slant opacity. Here, the molecular mixing ratio is a scaling factor to the total atmospheric number density defined by the temperature and pressure with the ideal gas assumption. In the fitting procedure, an optimal search is based on partial derivatives of the transmission on each of the free parameters. Here, the key contribution comes from the cross section derivative with respect to temperature: $/ T$ (Fig. 3b). The first guess values for the considered atmospheric parameters were taken from the Mars Climate Database (MCD 5.3; Millour et al., 2018) adopted for the ACS occultation climatology in MY 34 and 35.

Since the altitude, z, profiles of temperature $T(z)$ and CO_2 density $N_{CO2}(z)$ are simultaneously fitted, the pressure $p(z)$ is calculated by integrating $T(z)$ using the equation of hydrostatic equilibrium, assuming the ideal gas law. Once the hydrostatic pressure profile is derived, we keep it fixed when a new temperature and CO_2 density are retrieved on the next iteration. We repeat this procedure about 5-6 iterations while the profiles reach a convergence. Here, the values on an $(i\text{-}1)^{\text{th}}$ step are used as a priori for the i^{th} one. When sounding the CO_2-rich atmosphere by CO_2 spectroscopy, the fitting of N_{CO2} with the hydrostatic pressure assumption is physically reasonable, rather than using the directly fitted pressure while keeping N_{CO2} fixed.

The applied retrieval algorithm was performed for orders #222 and #223 separately since they require different calibration parameters with unique ILSs. Vertical profiles from order #223 were derived by Belyaev et al. (2021) and validated with analogous schemes, such as the one adopted by Alday et al. (2021a) using the NEMESIS algorithm and the one from ACS NIR (Fedorova et al., 2020) for simultaneous occultations at altitudes below 100 km. Comparison between the present MIR and the NIR temperature profiles is shown in Supplemental Figure S1, where a good consistency within ~10 K takes place. The profiles retrieved from order #223 are sensitive to altitudes from 5-20 km to 140-160 km (depending on season), while the profiles from #222 are sensitive to an altitude range ~20 km higher due to the stronger CO_2 lines. One of the uppermost transmission fits is presented in Figure 1a (zoomed inset) with

the absorption line depth not exceeding 0.2%. The lowest and the uppermost heights for an individual profile are established according to the retrieval uncertainties. These are estimated from the transmission errors and by a covariance matrix of the partial derivatives for all free parameters. We selected only the values corresponding to temperature error bars below 20 K. Final density and temperature profiles are obtained by "binding" those from both orders with a weighted average in the intersecting altitude interval (Figures 4a, 4e, 4i).

Together with the molecular abundance, we derive the aerosol slant opacity when fitting this parameter at the short wavelength edge of the order #223, i.e., at 3753-3755 cm^{-1}, where the gaseous absorption is minimal (Fig. 1). In our case, the opacity indicates the atmospheric aerosol loading along the LOS of ACS, expressing periods of the dust activity. Figure 4 demonstrates the retrieved vertical profiles from three different seasons: the global dust storm of MY 34 (4a-4d), perihelion of MY 34 (4e-4h), and aphelion of MY 35 (4i-4l) at the middle and high latitudes of the Southern Hemisphere. In the first two cases, the lower atmosphere is warmer (4b, 4f, 4j), denser (4c, 4g, 4k), and more dusty (4d, 4h, 4l) than in the third (aphelion) case. During the global dust storm (GDS) of 2018 (Montabone et al., 2020) the temperature bumps up to 210 K between 30 and 60 km (Fig. 4b), which correlates well with the correspondent aerosol detached layer (Fig. 4d). Perihelion, which occurs during the southern summer, is a period with intensified atmospheric upwelling and increased density and aerosol opacity (Fig. 4g, 4h). At the aphelion season, southern winter, the situation is opposite, with a colder and more transparent atmosphere (Fig. 4j-4l).

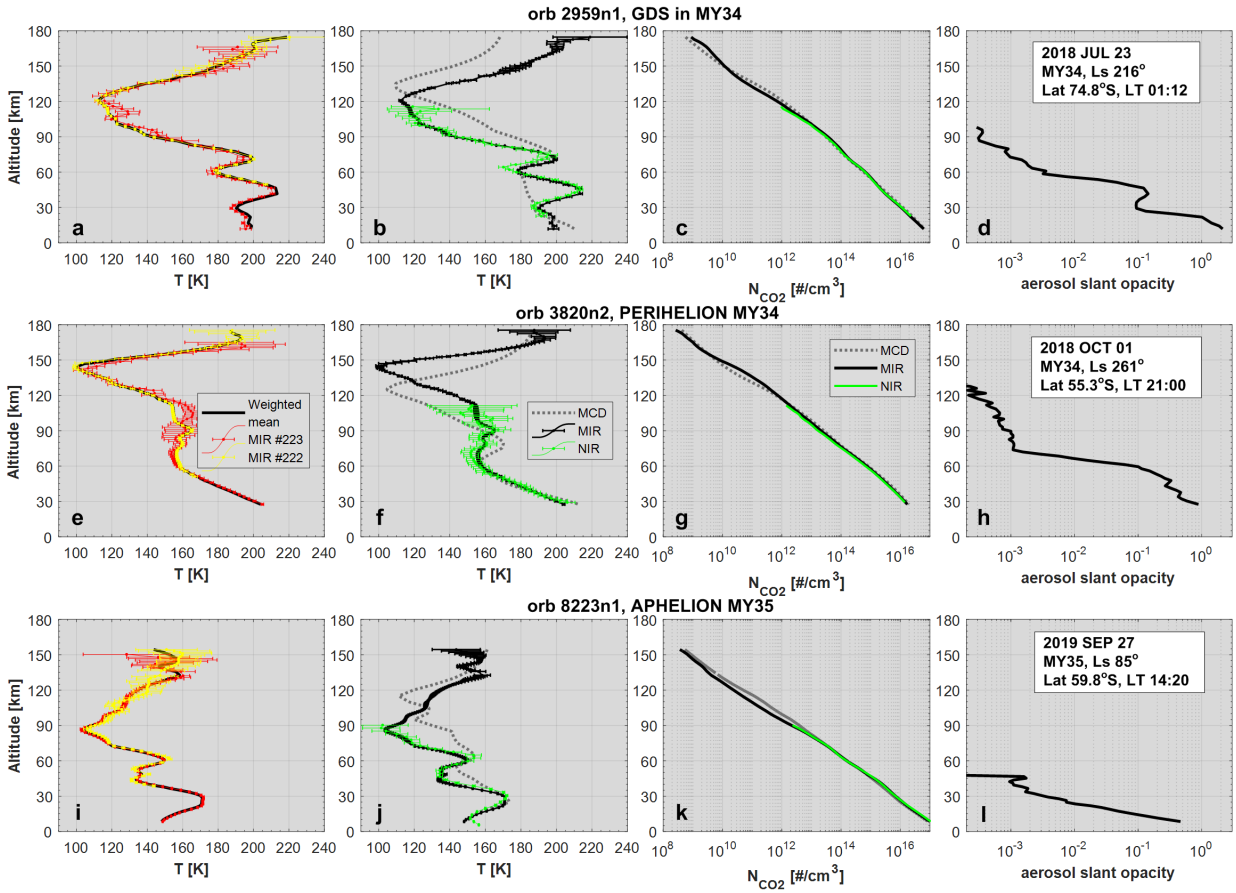

Figure 4. Individual vertical profiles of temperature (**a**, **b**, **e**, **f**, **i**, **j**), CO_2 number density (**c**, **g**, **k**), and aerosol slant opacity (**d**, **h**, **l**) retrieved from ACS MIR occultations in the Southern Hemisphere at different periods: Global dust storm in MY 34 (L_S = 216°; **a-d**), near perihelion in MY 34 (**e-h**), and near aphelion in MY 35 (**i-l**). Panels **a**, **e**, **i**: comparison between ACS MIR orders #222 (yellow) and #223 (red) with their weighted mean temperatures (black). Panels (**b**, **f**, **j**): comparison of the ACS MIR temperature profiles (black) with the ACS NIR ones (green; Fedorova et al., 2020) and with the MCD5.3 climatology predictions (gray). Panels **c**, **g**, **k**: analogous comparison for CO_2 number density.

4 Results

4.1 Mesopause altitude

In each individual vertical profile of the temperature, one can derive an altitude of the mesopause at the coldest point, for example, ~120 km (Fig. 4b), ~150 km (Fig. 4f), and ~90 km (Fig. 4j). The derived vertical profiles reveal that

over the whole data set this height varies in a broad altitude range, from 70 km to 150 km as seen in Figure 5. Here, the lowest mesopause altitude takes place at the end of the southern winter, in the middle latitudes of L_S = 120°-130°, where the black dots relate to the evening twilight. On the other hand, the uppermost mesopause altitude (up to 150 km) occurs in the summer time at high latitudes, in the south at perihelion and in the north at aphelion. Thus, a clear contrast in the latitudinal dependence is observed during solstice periods when the mesopause altitude decreases from the summer season (hemisphere) to the winter one (Fig. 5).

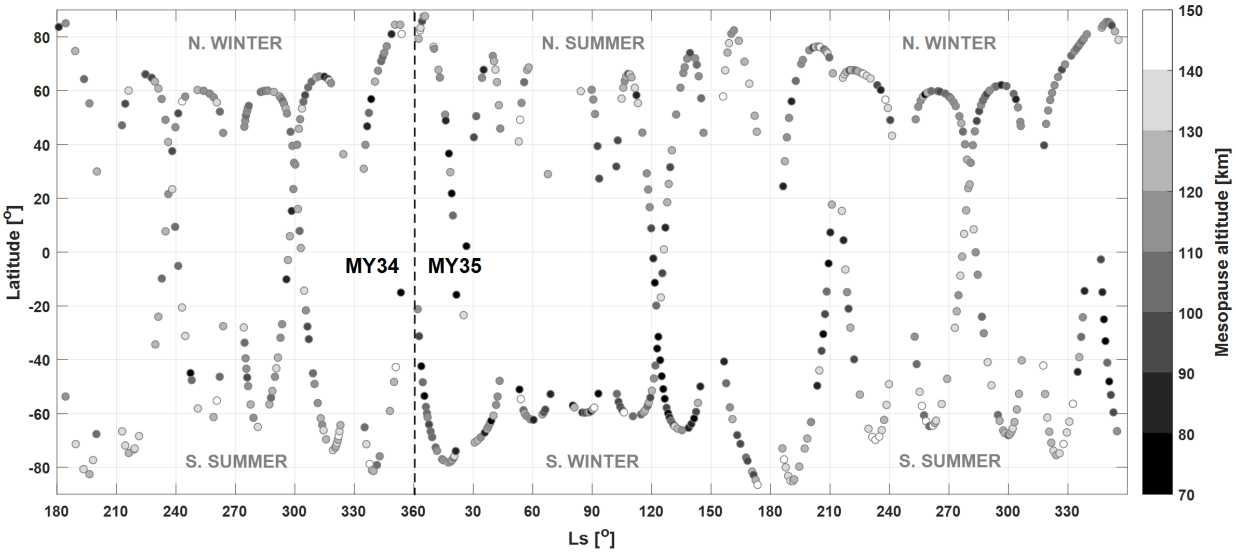

Figure 5. Gray-scale map of the mesopause altitude distribution with latitude and solar longitude (L_S) derived from ACS-MIR solar occultations for 1.5 Martian years.

4.2 Homopause altitude

The atmospheric homopause is the boundary between the homosphere, where the gaseous species are uniformly mixed with a common scale height, and the heterosphere, where a diffusive separation of minor species occurs with individual scale heights. The homopause altitude can be quantitatively determined when the eddy diffusion coefficient, which is dominant in the homosphere, equals the molecular diffusion coefficient, prevailing in the heterosphere. We calculated the vertical distribution of those coefficients from the retrieved density and temperature altitude profiles. Depending on a height, z, the eddy diffusion was estimated as $K(z) = K_0 \bullet \sqrt{\frac{n(20km)}{n(z)}}$, since the tropospheric eddy K_0 is equal to 10^6 cm^2/s at $z < 20$ km as it is assumed in 1D-models of Krasnopolsky (2019; p. 145). The total number density $n(z) = \frac{p(z)}{(k_B \bullet T(z))}$, where k_B is Boltzmann

constant, $T(z)$ is the temperature, and $p(z)$ is the hydrostatic pressure derived from the retrievals. If the lowest retrieved point exceeded 20 km, we linearly extrapolated the density profile (in log scale) down to 20 km, in order to reach the value n(20km).

The molecular diffusion coefficient D_{CO2}, being defined by the kinetic energy of molecule, is proportional to the free molecular path $l_{CO2}(z) = (Q_{CO2} \bullet n_{CO2}(z))^{-1}$ and to the mean thermal speed $v^{\mathrm{th}}_{CO2}(z) = \sqrt{\frac{3 \bullet k_B \bullet T(z) \bullet N_A}{M_{CO2}}}$, where Q_{CO2} is the CO_2 effective gas-kinetic cross section (0.52 nm^2), N_A is Avogadro number, and M_{CO2} is the CO_2 molar mass (44.01 g/mol). The complete expression is $D_{CO2}(z) = \frac{300\pi\sqrt{2}}{16} \bullet l_{CO2}(z) \bullet v^{\mathrm{th}}_{CO2}(z)$ as it is described by Jacobson (1999; p. 102, 528) and adopted by Mahieux et al. (2012) and Piccialli et al. (2015) for the CO_2-rich atmosphere of Venus.

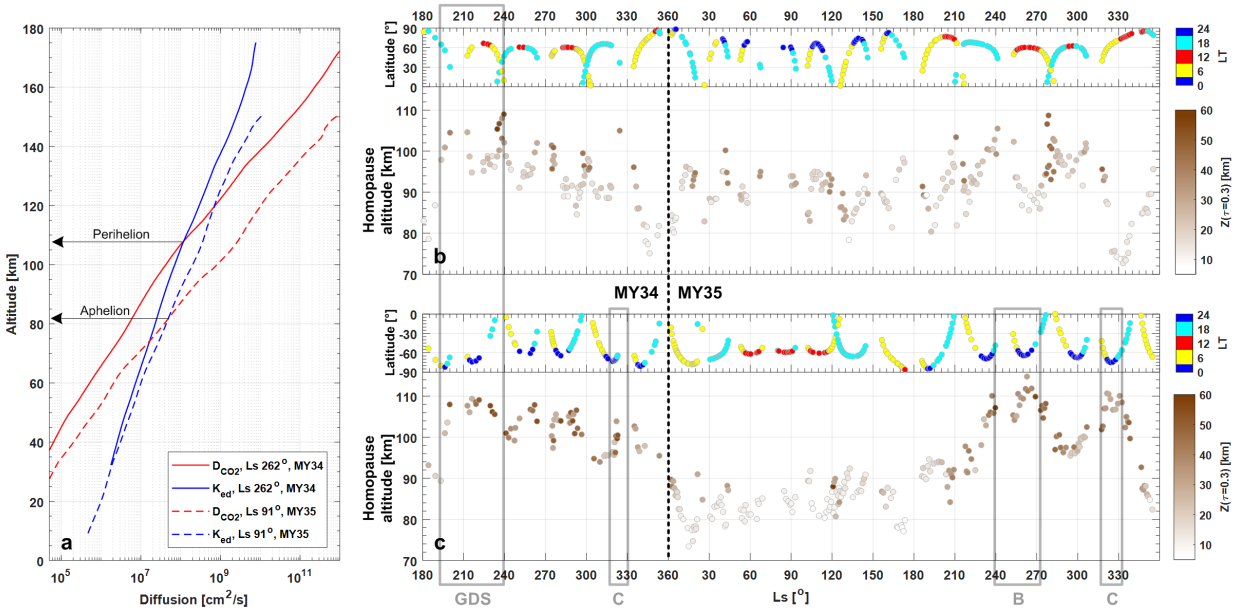

Figure 6. Revealing of the homopause altitude from the ACS MIR occultations for 1.5 Martian years. **a**: Vertical profiles of the molecular (D_{CO2}, in red) and eddy (K, in blue) diffusion coefficients retrieved from two the observations at perihelion MY 34 (solid lines) and aphelion MY 35 (dashed lines). Black arrows point to the definition of the homopause heights. **b**: Distribution of the homopause altitude versus solar longitude (L_S) in the Northern Hemisphere; the color code corresponds to an altitude Z level where the aerosol slant opacity ( ) equals 0.3. The data are supplemented by the latitudinal coverage taken from Figure 2c. **c**: Panel **b** shows the same for the Southern Hemisphere. Gray frames outline periods of the global dust storm (GDS) and the C storm in MY

34, and the B and C storms in MY 35.

Examples of the derived $K(z)$ and $D_{CO2}(z)$ profiles for the ACS MIR occultations at perihelion and aphelion are presented in Figure 6a. The homopause point is the height where correspondent $K(z)$ and $D_{CO2}(z)$ curves cross each other. In general, analyzing over 1.5 Martian years, this altitude varies from 80-90 km around aphelion to 95-105 km around perihelion in the Northern Hemisphere (Fig. 6b) and more sharply, to 100-110 km, in the Southern Hemisphere (Fig. 6c). Those local peaks in the general trends seem to correlate with the higher aerosol loading related to the dust seasons. It is expressed by an altitude level where the slant opacity equals 0.3 (that is ~75% of transmission). The higher this level, the denser the atmospheric aerosol densities, as can be estimated from the opacity profiles in Figures 4d, 4h, 4l. The homopause fluctuations are also defined by the latitudinal coordinates, as seen from the data coverage in Figures 6b and 6c. In parallel, the derived CO_2 number density at homopause varies from 10^{12} #/cm^3 at 110 km to 10^{13} #/cm^3 at 75 km.

Map of the homopause altitude distribution with latitude and solar longitude is presented in Figure 7. Here, the uppermost heights, above 105 km, correspond precisely to the distribution of dust events that took place during the considered 1.5 Martian years. The lowest homopause, below 80 km, occurs near the equinox polar regions in the morning twilight and at high southern winter latitudes.

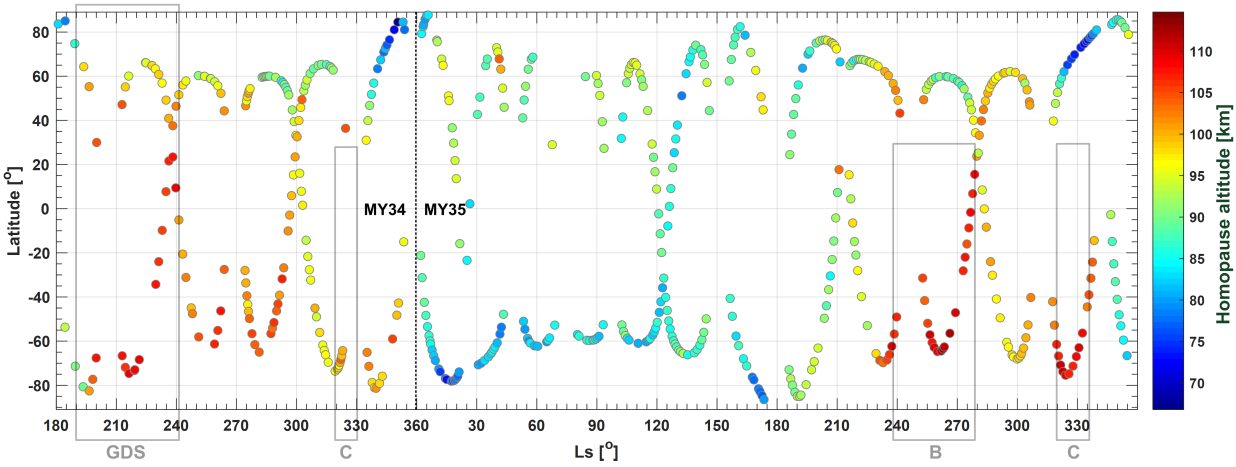

Figure 7. Colored map of the homopause altitude distribution with latitude and solar longitude (L_S) derived from ACS-MIR solar occultations for 1.5 Martian years. Gray frames outline periods of the global dust storm (GDS) and the C storm in MY 34, and the B and C storms in MY 35.

Alday et al. (2021b) also retrieved the altitude of homopause from the ACS MIR occultations when analyzing the fractionation by diffusive separation using vertical profiles of $^{13}C/^{12}C$ and $^{18}O/^{16}O$ isotopic ratios in CO_2. The derived

height occurred to be 95±2 km on average, which is consistent with our results. NGIMS onboard the MAVEN spacecraft observed the homopause variability in 2015-2016, between $L_S = 300°$ in MY 32 to $L_S = 250°$ in MY 33, using the density ratio of N_2 to Ar (Slipski et al., 2018). The minimum altitude was established at 70 km in the aphelion season, while the maximum at 130 km in the perihelion one, that is ~20 km higher than the uppermost ACS MIR values in Figures 6 and 7. The difference may relate to an increased solar flux in 2015 during dayside NGIMS measurements rather than our twilight occultations close to the solar minimum at 2018-2020 (Bougher et al., 2015a; Thiemann et al., 2018).

4.3 Climatology of CO_2 density vertical distribution

In order to study the seasonal variability of different atmospheric layers we grouped the vertical profiles in bins with intervals of 2° of L_S and 2 km of altitude. In such a way, each bin represents the weighted mean value from one to seven measured points. The points with 1-sigma temperature uncertainties larger than 20 K or relative density deviations exceeding 50% were excluded from consideration. The second rejection criterion corresponds to the detection limit of CO_2 number density ($5 \cdot 10^7$ cm^{-3}) that defines the seasonal variations of the uppermost detectable points. The distribution of CO_2 number density over 1.5 MYs is shown in Figure 6 for the Northern (8b) and Southern (8d) Hemispheres, separately. Those pictures are supplemented by the latitude coverage of individual occultations (Fig. 8a, 8c) with corresponding aerosol loading. Coordinates of the ACS MIR occultations just partially caught those storms, mainly at high latitudes, from which we can observe an altitude increase of several density layers during the mentioned events, especially in the Southern Hemisphere (Fig. 8c, 8d). Generally, seasonal variability for different density layers can be observed here. For example, a level of ~10^{12} cm^{-3} (black area in Figure 8), related to the mesopause and homopause layers, varies from 90-100 km at aphelion (L_S = 60°-120°) to 110-120 km at perihelion (L_S = 240°-300°).

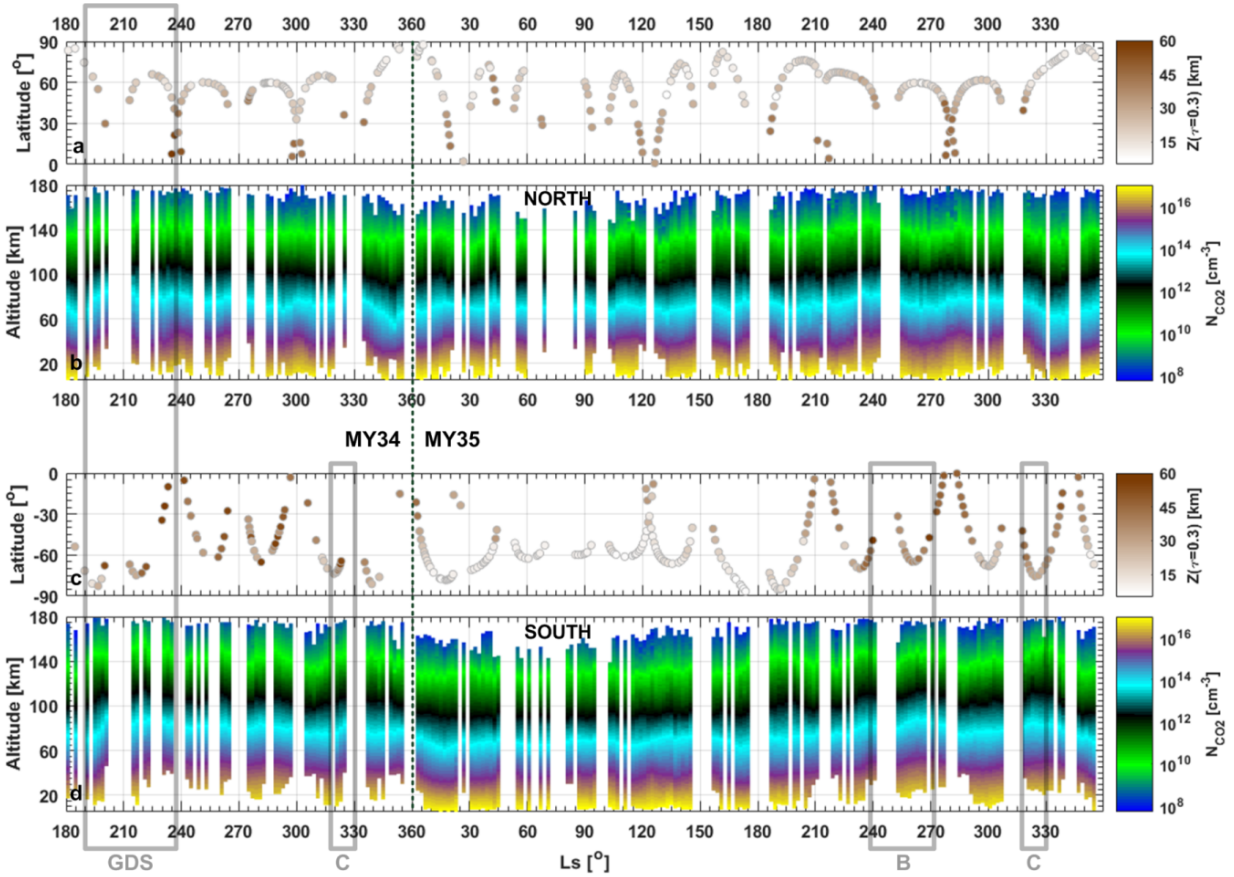

Figure 8. Solar longitude (L_S) cross-sections of ACS MIR temperature profiles, grouped in 2° bins, for the Northern (**b**) and Southern (**d**) Hemispheres. The density color code indicates different orders of magnitude on the logarithmic scale. Panels **a**, **c**: latitudinal distribution of the correspondent occultations colored as an altitude level Z where the aerosol slant opacity ( ) equals 0.3. Gray frames outline periods of the global dust storm (GDS) and the C storm in MY 34, and the B, C storms in MY 35.

Variability of the vertical density distribution depends on dust activity, on annual seasons, and it is also modulated by the latitude. To study the latitudinal behavior we grouped the vertical profiles in latitude bins of 5°. We combined the data together from MY 34 and MY 35 due to seasons in the the Southern Hemisphere (Fig. 9): autumn (L_S = 330°-30°), winter (L_S = 70°-130°), spring (L_S = 150°-210°), and summer (L_S = 240°-270°). The time intervals of stormy events were excluded from the consideration in order to make the equivalent contributions between both Martian years. The interval of southern winter is a bit shifted towards southern spring, in order to consider larger latitude coverage in this season. We also separate the profiles at midday (local time) due to the

difference between morning and evening terminators, as shown in Figure 2a.

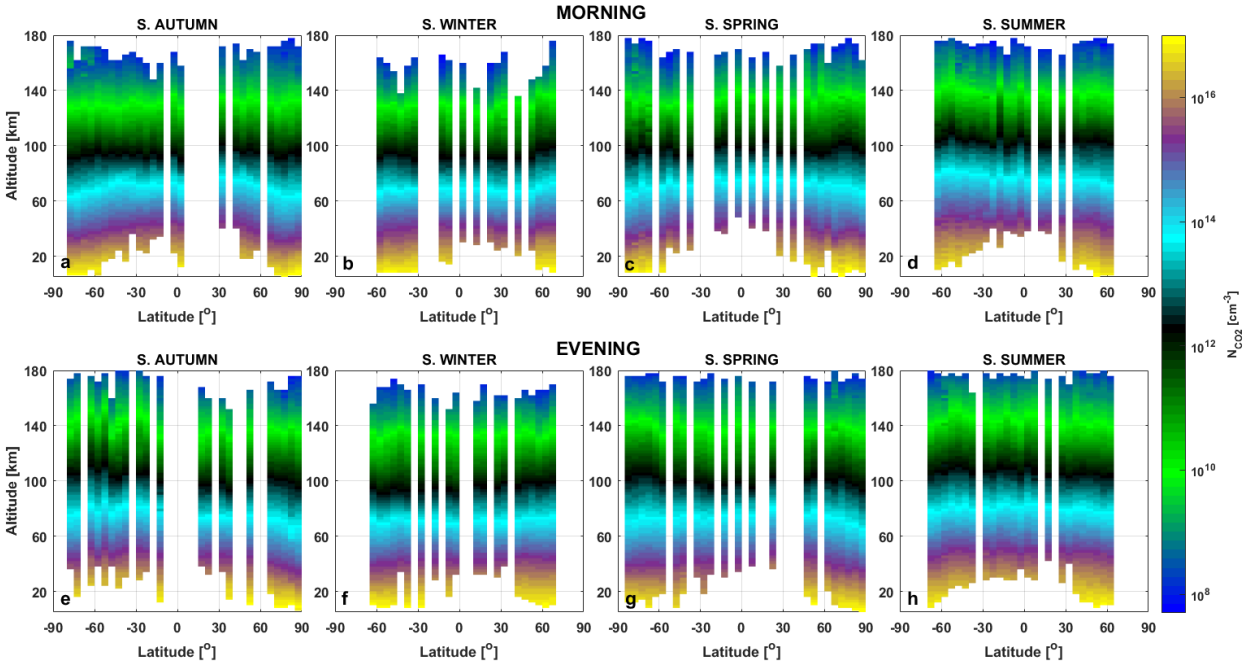

Figure 9. Latitude cross-sections of ACS MIR CO_2 density profiles, grouped in 5° bins corresponding to southern hemisphere seasons: s. autumn (**a, e**; L_S = 330°-30°), s. winter (**b, f**; L_S = 70°-130°), s. spring (**c, g**; L_S = 150°-210°), and s. summer (**d, h**; L_S = 240°-300°). The color code indicates different orders of magnitude of CO_2 density in the logarithmic scale. Data for the morning (**a-d**) and evening (**e-h**) terminators are separated on top and bottom respectively.

The latitudinal climatology reveals symmetrical decreases of the altitudes of equivalent CO_2 density layers from the equator to poles, below 120 km, during both autumn and spring seasons (Figures 9a, 9c, 9e, 9g). Southern winter and summer feature an asymmetry, where altitudes of equivalent density layers decrease from the north to the south in the southern winter (Figures 9b and 9f) and, reversely, from the south to the north in the southern summer (Figures 9d and 9h).

4.4 Climatology of temperature vertical distribution

Seasonal and latitudinal variations of the temperature vertical profiles were grouped in the same manner as for CO_2 density (Figures 8 and 9). In the current case, the distributions are supplemented by the latitudinal coverage colored by the local time (Figures 10a and 10c) in order to distinguish the thermal structures between the morning and evening twilight. The seasonal temperature variability is presented in Figure 10b for the Northern Hemisphere and in

Figure 10d for the Southern one. We observe peak temperatures in the middle atmosphere (40–80 km) during the GDS of MY 34, and a few smaller peaks at the regional B and C storms, regardless of their locations in high southern latitudes and close to the polar night time (Figures 10c and 10d). Apart from the distributions observed during the stormy periods, the middle atmosphere at perihelion (L_S = 240°-300°) is generally warmer than at aphelion (L_S = 60°-120°). Other mesospheric temperature peaks take place locally, depending on latitude. An example is the polar warming effect revealed near the equinox points (L_S = 330°-360° and L_S = 190°-210°, Figures 10a and 10b). The upper atmosphere features variations of the mesopause level at 70-150 km, indicating the coldest (dark blue) area in Figures 10b and 10d. The map characterizing seasonal distribution of the mesopause altitude versus latitude is presented in Figure 5. Above the mesopause, we observe the thermospheric temperature rise up to 250-260 K in the warmest case above 150 km.

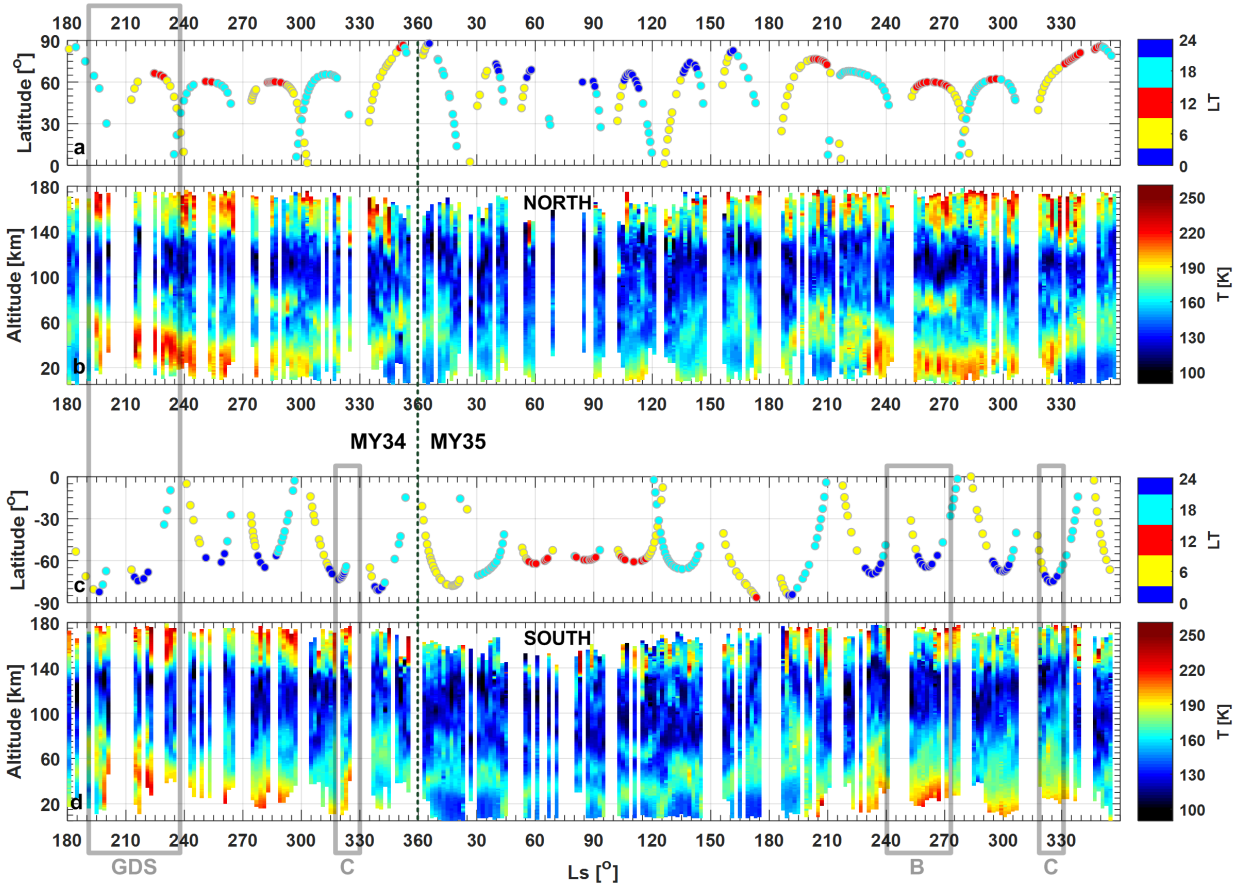

Figure 10. Solar longitude (L_S) cross-sections of ACS MIR temperature pro-

files, grouped in 2° bins, for the Northern (**b**) and Southern (**d**) Hemispheres. Panels **a**, **c**: latitudinal distribution of the correspondent occultations colored by local time (LT): morning (yellow), day (red), evening (purple), night (blue). Gray frames outline periods of the global dust storm (GDS) and the C storm in MY 34, and the B and C storms in MY 35.

In the latitudinal distributions, the mesospheric polar warming up to 160-190 K occurs at altitudes 50-90 km during autumn and spring in both hemispheres (Fig. 11a, 11c, 11e, 11g). Observing the middle thermosphere around 140-180 km at perihelion, one can reveal that the northern winter is warmer than the southern summer at the evening terminator at middle-high latitudes: 220-260 K versus 190-200 K, respectively (Fig. 11h). Analogous situation takes place in the morning southern autumn (Fig. 11a). The mesosphere and the lower thermosphere, at 70-140 km, indicate the mesopause distribution with latitude. One can point out the evening hours at the aphelion season (Fig. 11f), where a layer of the mesopause temperatures (100-120 K) falls down to 70-80 km at the middle southern latitudes (i.e. southern winter) and rises up to 110-120 km in the northern summer. Here, the atmosphere above 100 km is much warmer in the southern winter than in the northern summer, 140-160 K versus 100-120 K correspondingly.

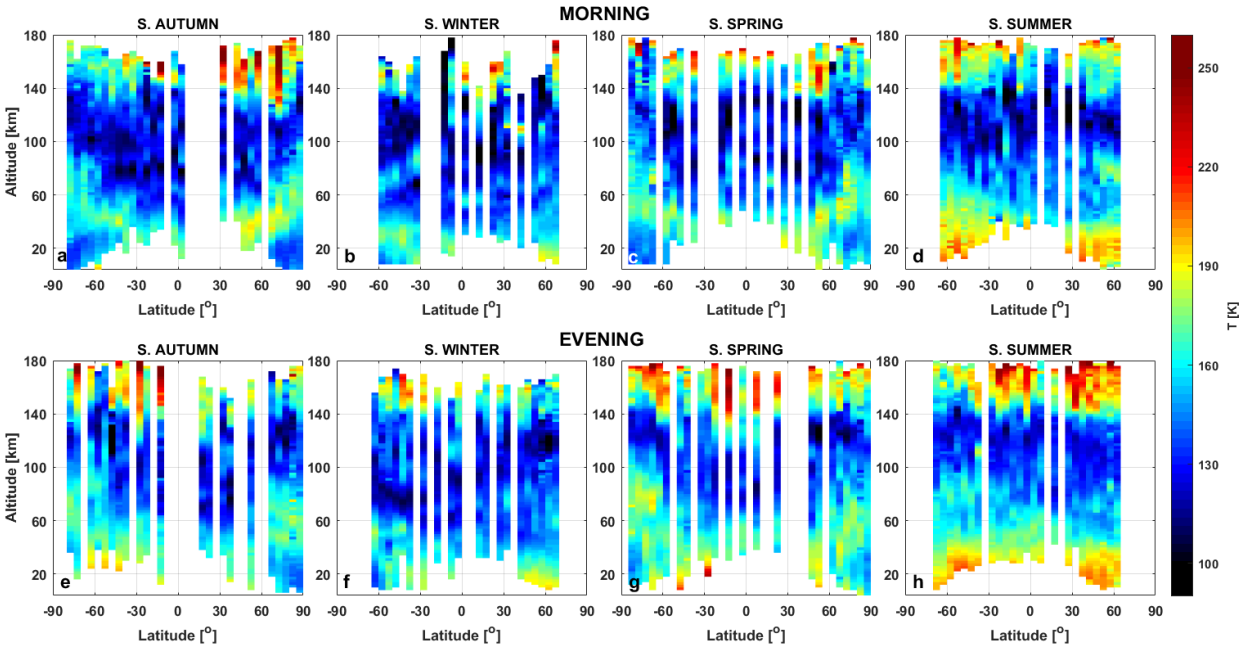

Figure 11. Latitude cross-sections of ACS MIR temperature profiles, grouped in 5° bins corresponding to southern hemisphere seasons: s. autumn (**a, e**; L_S = 330°-30°), s. winter (**b, f**; L_s = 70°-130°), s. spring (**c, g**; L_S = 150°-210°),

and s. summer (**d, h**; L_S = 240°-300°). The color code indicates different temperatures. Data for the morning (**a-d**) and evening (**e-h**) terminators are separated on top and bottom.

The Martian global climate model interprets the winter warming up to >200 K on both Poles in the thermosphere above 140 km as a result of intense global circulation and in-situ tides (González-Galindo et al., 2009, 2015, 2017). ACS MIR observes this effect at middle-high latitudes in the northern winter (perihelion, Figures 11d and 11h), up to 200-220 K, and in the southern one (aphelion, Fig. 11f), up to 180-190 K. Before, the MGS aerobraking around 120 km also revealed the warmer perihelion winter (L_S ~ 270°, ~160 K) than the aphelion winter (L_S ~ 90°, ~140 K) (Bougher et al., 2006). The authors explained this behavior by the stronger insolation and dust heating near perihelion. The exospheric polar and mid-latitude warming up to 250 K at perihelion was also observed by the EUVM/MAVEN solar occultations above 150 km (Thiemann et al., 2018). The SPICAM stellar occultations demonstrated a polar warming on the night side at altitudes below the mesopause during the period L_S = 120°-150° (Forget et al., 2009). Our observations in this seasonal interval, lying between southern winter and spring, reach latitudes not higher than 70° in both hemispheres (see Figure 10) with consistent warming, up to 150-170 K below the mesopause.

5 Conclusions

For the first time, we report the atmospheric density and temperature retrievals in an extremely broad altitude range from 20 to 180 km on a basis of the CO_2 infrared absorption spectroscopy in the Martian atmosphere. We have used solar occultation measurements by the ACS MIR spectrometer, which is highly sensitive to the strong rotational absorption band of carbon dioxide at the wavelength of 2.7 m. The retrieval scheme of the transmission spectra include the simultaneous characterization of the CO_2 density and temperature vertical profiles under the assumption of hydrostatic equilibrium. We have processed more than 600 occultation sessions encompassing different seasons over 1.5 Martian years, the second half of MY 34 and the whole of MY 35. This allowed deriving the seasonal and latitudinal climatology of the density and temperature profiles in both hemispheres and either at morning or at evening terminators.

In the behavior of different atmospheric layers, one can highlight the following features:

- An increase of the temperature and CO_2 density in the lower-middle atmosphere (below ~100 km) during several dust events, including GDS at L_S = 190°-240° in MY 34 and further B and C storms in MY 35.
- A symmetrical decrease of equal CO_2 density altitude layers from the equator to poles in spring and autumn.
- The mesospheric polar warming up to 160-190 K at altitudes 50-90 km during spring and autumn; in the thermosphere such a warming is observed on both northern and southern winter seasons at the middle-high

latitudes.

- The mesopause altitude varies in a large range, rising from 70-90 km in the winter high latitudes to 130-150 km in the summer high latitudes.
- The homopause altitude varies from 80-90 km at aphelion to 100-110 km at perihelion; some local variations are defined depending on dust activity. The correspondent CO_2 density at the homopause is found to be 10^{12}–10^{13} #/cm^3.

All in all, we have presented a wide diagnostic potential for the troposphere, the mesosphere and the thermosphere of Mars by the ACS MIR spectroscopy at the CO_2 2.7 m band. The retrieved data set in the middle and upper atmosphere can serve as a reference for comparison with existing circulation models, e.g., one of González-Galindo et al. (2015) or of Medvedev et al. (2015), and improve them. In particular, the observed effects of polar warming have been already predicted by those models and could be compared quantitatively.

Apart from the mentioned features in the climatology, gravity waves (GW) can be spotted as harmonic oscillations in the temperature and density vertical profiles. The GW activity was observed several times by descent and aerobraking probes, as well as remotely by stellar occultations (see in Introduction and Vals et al. (2019)). In the ACS MIR atmospheric profiles, possessing a rather tiny vertical resolution of 1-2 km, Starichenko et al. (2021) derived the GW parameters, such as amplitude, wavenumbers and the Brunt-Vaissalla frequency, expressing the atmospheric stability. Those retrievals cover the second half MY 34 with the MIR echelle order #223, related to altitudes up to 140-160 km. The current enhanced observations, up to 160-180 km and until the end of MY 35, enrich the GW climatology including aphelion and perihelion of MY 35 that will contribute to the correspondent circulation models (Medvedev et al., 2011; 2019).

Acknowledgments

ExoMars is a joint space mission of the European Space Agency (ESA) and Roscosmos. The ACS experiment is led by the Space Research Institute (IKI) in Moscow, assisted by LATMOS in France. The analysis of temperature and density profiles at IKI are funded by the grant #20-42-09035 of the Russian Science Foundation. Oxford participants acknowledge funding from the UK Space Agency (ST/T002069/1) for the data validation.

Data Availability Statement

The data sets generated by the ExoMars Trace Gas Orbiter instruments analyzed in this study are available in theESA Planetary Science Archive (PSA) repository, https://archives.esac.esa.int/psa/#!Table%20View/ACS=instrument, following a six months prior access period, following the ESA Rules on Information, Data and Intellectual Property. The data products generated in this

study (retrieved CO_2 density and temperature distributions) are available on Belyaev (2022).

References

Alday, J., Wilson, C. F., Irwin, P. G. J., Olsen, K. S., Baggio, L., Montmessin, F., et al. (2019). Oxygen isotopic ratios in Martian water vapor observed by ACS MIR on board the ExoMars Trace Gas Orbiter. *Astronomy and Astrophysics, 630*, A91. https://doi.org/10.1051/0004-6361/201936234.

Alday, J., Trokhimovskiy, A., Irwin, P. G. J., Wilson, C. F., Montmessin, F., Lefevre, F., et al. (2021a). Isotopic fractionation of water and its photolytic products in the atmosphere of Mars. *Nature Astronomy*, *5*, 943–950. https://doi.org/10.1038/s41550-021-01389-x.

Alday, J., Wilson, C. F., Irwin, P. G. J., Trokhimovskiy, A., Montmessin, F., Fedorova, A. A., et al. (2021b). Isotopic composition of CO_2 in the atmosphere of Mars: Fractionation by diffusive separation observed by the ExoMars Trace Gas Orbiter. *Journal of Geophysical Research: Planets*, *126*, e2021JE006992. https://doi.org/10.1029/2021JE006992.

Avduyevskiy, V. S., E. L. Akim, V. I. Aleshin, et al. (1975). Martian atmosphere in the landing site of the descent module of Mar- 6. *NASA transl. into English from Kosm. Issled. (USSR), 13*, 1, January– February, 21– 32.

Belyaev, D. A., Fedorova, A. A., Trokhimovskiy, A., Alday, J., Montmessin, F., Korablev, O. I., et al. (2021). Revealing a high water abundance in the upper mesosphere of Mars with ACS onboard TGO. *Geophysical Research Letters*, *48*, e2021GL093411. https://doi.org/10.1029/2021GL093411.

Belyaev, D. (2022). *Thermal Structure of the Middle and Upper Atmosphere of Mars from ACS/TGO CO_2 Spectroscopy.* Mendeley Data, V1, doi: 10.17632/g6j5t2z73z.1.

Bougher, S. W., Bell, J. M., Murphy, J. R., Lopez-Valverde, M. A., & Withers, P. G. (2006). Polar warming in the Mars thermosphere: Seasonal variations owing to changing insolation and dust distributions, *Geophysical Research Letters*, *33*, L02203, https://doi.org/10.1029/2005GL024059.

Bougher, S. W., Pawlowski, D., Bell, J. M., Nelli, S., McDunn, T., Murphy, J. R., Chizek, M., & Ridley, A. (2015a). Mars Global Ionosphere-Thermosphere Model (MGITM): Solar cycle, seasonal, and diurnal variations of the Mars upper atmosphere. *J. Geophys. Res.: Planets, 120*, 311–342, doi:10.1002/2014JE004715.

Bougher, S., et al. (2015b). Early MAVEN Deep Dip campaign reveals thermosphere and ionosphere variability. *Science*, *350*(6261), doi: 10.1126/science.aad0459.

Bougher, S., et al. (2017a). Chapter 14: Upper Atmosphere and Ionosphere, in *The Atmosphere and Climate of Mars*, ed. B. Haberle, M. Smith, T. Clancy, F. Forget, R. Zurek, Cambridge University Press, https://doi.org/10.1017/9781107016187.

Bougher, S. W., Roeten, K., Olsen, K., Mahaffy, P. R., Benna, M., Elrod, M., et al. (2017b). The structure and variability of Mars dayside thermosphere from MAVEN NGIMS and IUVS measurements: Seasonal and solar activity trends in scale heights and temperatures, *Journal of Geophysical Research: Space Physics*, 122, 1296-1313. https://doi.org/10.1002/2016JA023454.

Devi, V. M., Benner, D. C., Sung, K., Crawford, T. J., Gamache, R. R., Renaud, C. L., et al. (2017). Line parameters for CO_2- and self-broadening in the 3 band of $HD^{16}O$. *Journal of Quantitative Spectroscopy and Radiative Transfer*, *203*, 158–174. https://doi.org/10.1016/j.jqsrt.2017.02.020.

Fedorova, A. A., et al. (2020). Stormy water on Mars: The distribution and saturation of atmospheric water during the dusty season. *Science*, *367*(6475), 297–300. https://doi.org/10.1126/science.aay9522.

Forbes, J. M., Bruinsma, S., Zhang, X., Forget, F., Marty, J.-C., Millour, E., & Gonsalez-Galindo, F. (2021). The wave origins of longitudinal structures in ExoMars Trace Gas Orbiter (TGO) aerobraking densities. *Journal of Geophysical Research: Space Physics*, *126*, e2020JA028769. https://doi.org/10.1029/2020JA028769.

Forget, F., Montmessin, F., Bertaux, J.-L., González-Galindo, F., Lebonnois, S., Quémerais, E., Reberac, A., Dimarellis, E., & López-Valverde, M. A. (2009). Density and temperatures of the upper Martian atmosphere measured by stellar occultations with Mars Express SPICAM. *Journal of Geophysical Research*, *114*, E01004, https://doi.org/10.1029/2008JE003086.

Fu, M. H., Cui, J., Wu, X. S., Wu, Z. P., & Li, J. (2020). The variations of the Martian exobase altitude. *Earth Planetary Physics*, *4*(1), 4–10. http://doi.org/10.26464/epp2020010.

Gamache, R. R., Farese, M., & Renaud, C. L. (2016). A spectral line list for water isotopologues in the 1100-4100 cm^{-1} region for application to CO_2-rich planetary atmospheres. *Journal of Molecular Spectroscopy*, *326*, 144–150. https://doi.org/10.1016/j.jms.2015.09.001.

Gonzalez-Galindo, F., Forget, F., Lopez-Valverde, M. A., & Angelats i Coll, M. (2009). A ground-to-exosphere Martian general circulation model: 2. Atmosphere during solstice conditions - Thermospheric polar warming. *Journal of Geophysical Research*, *114*, E08004. https://doi.org/10.1029/2008JE003277.

González-Galindo, F., et al. (2015). Variability of the Martian thermosphere during eight Martian years as simulated by a ground-to-exosphere global circulation model. *Journal of Geophysical Research: Planets*, *120*(11), 2020-2035.

Gordon, I. E., Rothman, L. S., Hill, C., Kochanov, R. V., Tan, Y., Bernath, P. F., et al. (2017). The HITRAN2016 molecular spectroscopic database. *Journal of Quantum Spectroscopy and Radiative Transfer*, *203*, 3–69. https://doi.org/10.1016/j.jqsrt.2017.06.038.

Gröller, H., Montmessin, F., Yelle, R. V., Lefevre, F., Forget, F., Schneider, N. M., et al. (2018). MAVEN/IUVS stellar occultation measurements of Mars atmospheric structure and composition. *Journal of Geophysical Research: Planets*, *123*, 1449–1483. https://doi.org/10.1029/2017JE005466.

Jacobson, M. Z (2005). *Fundamentals of atmospheric modeling.* NY: Cambridge University Press, 2nd edition 2005. https://doi.org/10.1017/CBO9781139165389.

Jain, S. K., Soto, E., Evans, J. S., Deighan, J., Schneider, N. M., & Bougher, S. W., et al. (2021). Thermal structure of Mars' middle and upper atmospheres: Understanding the impacts of dynamics and of solar forcing. *Icarus*, https://doi.org/10.1016/j.icarus.2021.114703.

Jesch, D., Medvedev, A. S., Castellini, F., Yigit, E., & Hartogh, P. (2019). Density fluctuations in the lower thermosphere of Mars retrieved from the ExoMars Trace Gas Orbiter (TGO) aerobraking. *Atmosphere*, *10*, 620, https://doi.org/10.3390/atmos10100620.

Kass, D. M., Kleinböhl, A., McCleese, D. J., Schofield, J. T., & Smith M. D. (2016). Interannual similarity in the Martian atmosphere during the dust storm season. *Geophysical Research Letters*, *48*(12), https://doi.org/10.1002/2016GL068978.

Keating, G. M., Bougher, S. W., Zurek, R. W., Tolson, R. H., Cancro, G. J., Noll, S. N., & Murphy, J. R. (1998). The structure of the upper atmosphere of Mars: In situ accelerometer measurements from Mars Global Surveyor. *Science*, 279(5357), 1672-1676.

Krasnopolsky, V. A. (2019). *Spectroscopy and photochemistry of planetary atmospheres and ionospheres: Mars, Venus, Titan, and Pluto.* NY: Cambridge University Press, 2019. https://doi.org/10.1017/9781316535561.

Korablev, O. I., Montmessin, F., Trokhimovskiy, A., Fedorova, A. A., Shakun, A. V., Grigoriev, A. V., et al. (2018). The Atmospheric Chemistry Suite (ACS) of three spectrometers for the ExoMars 2016 trace gas orbiter. *Space Science Reviews*, *214*(1). https://doi.org/10.1007/s11214-017-0437-6.

Medvedev, A. S., Yiğit, E., Hartogh, P., & Becker, E. (2011). Influence of gravity waves on the Martian atmosphere: General circulation modeling. *Journal of Geophysical Research*, *116*(E10004). https://doi.org/10.1029/2011JE003848.

Medvedev, A. S., González-Galindo, F., Yiğit, E., Feofilov, A. G., Forget, F., & Hartogh, P. (2015). Cooling of the Martian thermosphere by CO_2 radiation and gravity waves: An intercomparison study with two general circulation models. *Journal of Geophysical Research: Planets*, *120*(5), 913-927. https://doi.org/10.1002/2015JE004802.

Medvedev, A. S., & Yiğit, E. (2019). Gravity waves in planetary atmospheres: Their effects and parameterization in global circulation models. *Atmosphere*, *10*(9), 531. https://doi.org/10.3390/atmos10090531.

Millour, E., Forget, F., Spiga, A., Vals, M., Zakharov, V., Montabone, L., et al. (2018). *The Mars Climate Database (Version 5.3).* The Mars Climate Database Science Workshop "from Mars Express to ExoMars", held 27-28 February 2018 at ESAC, Spain, id.68. https://www.cosmos.esa.int/documents/1499429/1583871/Millour_E.pdf/ca419d58-4c0b-29a4-23a9-7c814b5e889e?t=1516102807000

Montabone, L., Spiga, A., Kass, D. M., Kleinböhl, A., Forget, F., & Millour, E. (2020). Martian Year 34 column dust climatology from Mars Climate Sounder observations: Reconstructed maps and model simulations. *Journal of Geophysical Research: Planets*, *125*(8), e06111. https://doi.org/10.1029/2019JE006111.

Montmessin, F., Bertaux, J.-L., Quémerais, E., Korablev, O., Rannou, P., Forget, F., Perrier, S., Fussen, D., Lebonnois, S., Rébérac, A., & Dimarellis, E. (2006). Subvisible CO_2 ice clouds detected in the mesosphere of Mars. *Icarus*, *183*(2), 403-410. https://doi.org/10.1016/j.icarus.2006.03.015.

Nakagawa, H., Terada, N., Jain, S. K., Schneider, N. M., Montmessin, F., Yelle, R. V., et al. (2020). Vertical propagation of wave perturbations in the middle atmosphere on Mars by MAVEN/IUVS. *Journal of Geophysical Research: Planets*, *125*, e2020JE006481. https://doi.org/10.1029/2020JE006481.

Olsen, K.S., Trokhimovskiy, A., Montabone, L., Fedorova, A.A., Luginin, M., Lefèvre, F., Korablev, O. I., Montmessin, F., Forget, F., Millour, E., Bierjon, A., Baggio, L., Alday, J., Wilson, C. F., Irwin, P. G. J., Belyaev, D. A., Patrakeev, A., & Shakun, A. (2021). Seasonal reappearance of HCl in the atmosphere of Mars during the Mars year 35 dusty season. *Astronomy & Astrophysics*, *647,* A161. https://doi.org/ 10.1051/0004-6361/202140329.

Piccialli, A., Montmessin, F., Belyaev, D., Mahieux, A., Fedorova, A., Marcq, E., Bertaux, J.-L., Vandaele, A.-C., Korablev, O. (2015). Thermal structure of Venus nightside upper atmosphere measured by stellar occultations with SPICAV/Venus Express. *Planetary and Space Science*, *113–114*, 321-335. http://dx.doi.org/10.1016/j.pss.2014.12.009.

Quemerais, E., et al. (2006). Stellar occultations observed by SPICAM on Mars Express. *Journal of Geophysical Research*, *111*, E09S04. https://doi.org/10.1029/2005JE002604.

Slipski, M., Jakosky, B. M., Benna, M., Elrod, M., Mahaffy, P., Kass, D., Stone, S., & Yelle, R. (2018). Variability of Martian turbopause altitudes. *Journal of Geophysical Research: Planets.. 123*(11), 2939-2957. https://doi.org/10.1029/2018JE005704.

Starichenko, E. D., Belyaev, D. A., Medvedev, A. S., Fedorova, A. A., Korablev, O. I., Trokhimovskiy, A., et al. (2021). Gravity wave activity in the Martian atmosphere at altitudes 20–160 km from ACS/TGO occultation

measurements. *Journal of Geophysical Research: Planets*, *126*, e2021JE006899. https://doi.org/10.1029/2021JE006899.

Stone, S., et al. (2018). Thermal structure of the Martian upper atmosphere from MAVEN NGIMS. *Journal of Geophysical Research: Planets*, *123*, 2842–2867. https://doi.org/10.1029/2018JE005559.

Thiemann, E. M. B., Eparvier, F. G., Bougher, S. W., Dominique, M., Andersson, L., Girazian, Z., et al. (2018). Mars thermospheric variability revealed by MAVEN EUVM solar occultations: Structure at aphelion and perihelion and response to EUV forcing. *Journal of Geophysical Research: Planets, 123*, 2248–2269. https://doi.org/10.1029/2018JE005550.

Vals, M., Spiga, A., Forget, F., Millour, E., Montabone, L., & Lott, F. (2019). Study of gravity waves distribution and propagation in the thermosphere of Mars based on MGS, ODY, MRO and MAVEN density measurements. *Planetary and Space Science*, *178*, 104708. https://doi.org/10.1016/j.pss.2019.104708.

Vandaele, A.-C., et al. (2018). NOMAD, an integrated suite of three spectrometers for the ExoMars Trace Gas Mission: technical description, science objectives and expected performance. *Space Science Reviews*, *214*, 80. https://doi.org/10.1007/s11214-018-0517-2.

Withers, P., Towner, M. C., Hathi, B., & Zarnecki, J. C. 2003. Analysis of entry accelerometer data: A case study of Mars Pathfinder. *Planetary and Space Science*, *51*, 9–10, pp. 541-561. https://doi.org/10.1016/S0032-0633(03)00077-1.

Withers, P. (2006). Mars Global Surveyor and Mars Odyssey Accelerometer observations of the Martian upper atmosphere during aerobraking. *Geophysical Research Letters*, *33*(2), L02201, https://doi.org/ 10.1029/2005GL024447.

Zurek, R. W., Tolson, R. A., Bougher, S. W., Lugo, R. A., Baird, D. T., Bell, J. M., & Jakosky, B. M. (2017). Mars thermosphere as seen in MAVEN accelerometer data. *Journal of Geophysical Research: Space Physics*, *122*(3), 3798-3814.